Title	Measurements of nonequilibrium interatomic forces using time-domain x-ray scattering
Authors	Teitelbaum, Samuel W.;Henighan, Thomas C.;Liu, Hanzhe;Jiang, Mason P.;Zhu, Diling;Chollet, Matthieu;Sato, Takahiro;Murray, Éamonn D.;Fahy, Stephen B.;O'Mahony, Shane;Bailey, Trevor P.;Uher, Ctirad;Trigo, Mariano;Reis, David A.
Publication date	2021-05-18
Original Citation	Teitelbaum, S. W., Henighan, T. C., Liu, H., Jiang, M. P., Zhu, D., Chollet, M., Sato, T., Murray, E. D., Fahy, S. B., O'Mahony, S., Bailey, T. P., Uher, C., Trigo, M. and Reis, D. A. (2021) 'Measurements of nonequilibrium interatomic forces using time-domain x-ray scattering', Physical Review B, 103(3), L180101 (6pp). doi: 10.1103/PhysRevB.103.L180101
Type of publication	Article (peer-reviewed)
Link to publisher's version	10.1103/PhysRevB.103.L180101
Rights	© 2021, American Physical Society. All rights reserved.
Download date	2024-04-20 04:00:55
Item downloaded from	https://hdl.handle.net/10468/12328

Supplemental Information For: Measurements of Nonequilibrium Interatomic Forces using Time-Domain X-ray Scattering

Samuel W. Teitelbaum,[1,2] Samuel W. Teitelbaum,[1,2] Thomas C. Henighan,[1,3] Hanzhe Liu,[1,3] Mason P. Jiang,[3,1] Diling Zhu,[4] Matthieu Chollet,[4] Takahiro Sato,[4] Éamonn D. Murray,[5] Stephen Fahy,[6,7] Shane O'Mahony,[6,7] Trevor P. Bailey,[8] Ctirad Uher,[8] Mariano Trigo,[1,2] and David A. Reis[1,2,9,10]

[1]*PULSE Institute of Ultrafast Energy Science, SLAC National Accelerator Laboratory, Menlo Park, California 94025, USA*

[2]*Stanford Institute for Materials and Energy Sciences, SLAC National Accelerator Laboratory, Menlo Park, California 94025, USA*

[3]*Department of Physics, Stanford University, Stanford, California 94305, USA*

[4]*Linac Coherent Light Source, SLAC National Accelerator Laboratory, Menlo Park, California 94025, USA*

[5]*Department of Physics and Department of Materials, Imperial College London, London SW7 2AZ, United Kingdom*

[6]*Tyndall National Institute, Cork, Ireland*

[7]*Department of Physics, University College Cork, Cork, Ireland*

[8]*Department of Physics, University of Michigan, Ann Arbor, Michigan 48109, USA*

[9]*Department of Applied Physics, Stanford University, Stanford, California 94305, USA*

[10]*Department of Photon Science, Stanford University, Stanford, California 94305, USA*

SUPPLEMENTAL INFORMATION

The supplemental information provides additional information about the fitting routine, the extraction of the interatomic forces from the geometry, and the time and frequency-domain datasets.

Fitting Routine for Phonon Frequencies

As described in the main text, the time-domain data was collected on the Cornell-SLAC pixel array detector (CSPAD). The arrival-time corrected data forms a three-dimensional array of 1691 by 1692 reciprocal space points by 152 time points spaced in 40 fs steps, over a span of 5.96 ps. An example frame is shown in fig. 1(a). Each time point detector frame was interpolated from a 1691 by 1692 image to a 256 by 256 by 152 array for fitting. Representative traces of the interpolated array are shown in fig. 1(b).

We begin with the reduced 256 by 256 (reciprocal space) by 154 (time) pixel array. For each pixel, linear prediction fitting (LPF) using six components returns one to two values with nonzero frequency. Linear prediction fitting fits a time-domain signal $S(t)$ to a sum of M exponentially damped oscillators

$$S(t) = \sum_{i=1}^{M} A_i e^{-\Gamma_i t} \cos\left(2\pi f_i t + \phi_i\right) \tag{1}$$

The number of oscillators used in the LPF fitting is half the number of components with nonzero frequencies (because each component with nonzero frequency contains a sine and cosine component). Therefore, LPF with six components includes two exponential decays, and up to two oscillating components (with sine and cosine amplitudes). Of the two oscillating components, we assign any components between 0.1 and 2 THz to an acoustic mode. This eliminates the contributions of the A_{1g} mode at 2.5-3 THz (depending on the excitation fluence) and the zero and low-frequency components associated with a quasi-DC increase in scattering intensity. Representative fits to the time-domain data are shown as black lines in fig. 1

Statistical uncertainties in the fitted frequency as a function of reduced pixel were obtained by performing the fitting routine above for three subsets of the lowest fluence data, with each subset containing 30 experimental runs each out of the 120 total runs used in

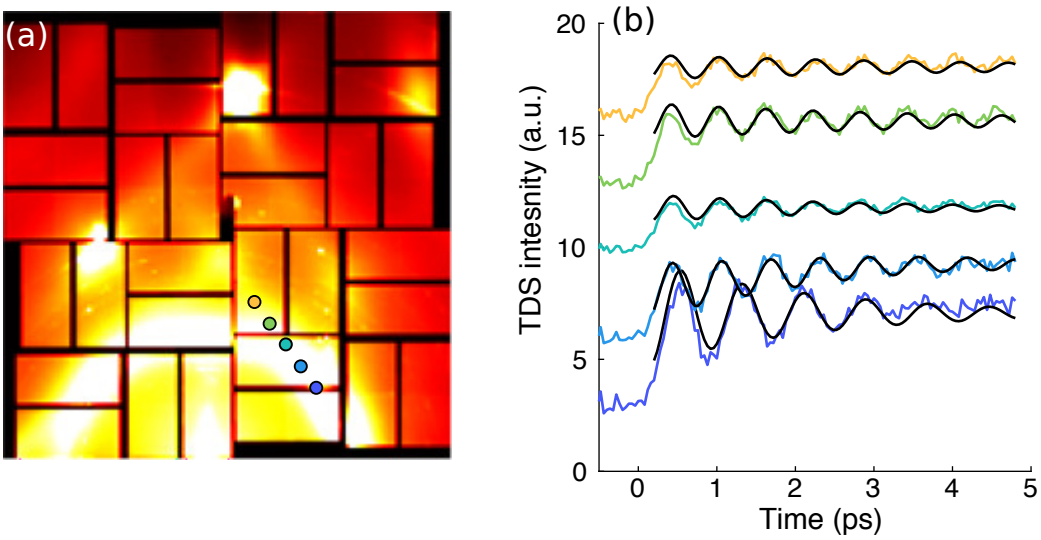

FIG. 1. (a) equilibrium diffuse scattering image of bismuth in our experimental geometry. Intensity scale is linear. Points correspond to traces of the same color in (b), which is along the linecut shown in the fig. 1(a) inset. (b) Time-domain diffuse scattering traces. Fits to LPF are shown as black lines overlaid on the time-domain data.

the final analysis. The uncertainty is defined as half-width between the largest and smallest fitted frequencies.

The extracted frequencies as over the detector image are shown in fig. 2(a). Selected Brillouin zone indices are also labeled.

Fitting Routine for Interatomic Forces

The model is fit by optimizing the adjustable force eigenvalues, which are defined as the vector X, with $3N_{IFC}$ components, where N_{IFC} is the number of force matrices used. The fit result is the vector X that minimizes the least-squares error (eq. 2) for all detector pixels for which the linear prediction fitting converges. The least-squares fitting of the observed frequency f_n for all N pixels n on the detector with an observed frequency is the optimized reduced mean-square error (MSE),

$$\chi^2(\boldsymbol{X}) = \frac{1}{N - n_X} \sum_{n=1}^{N} \left(\frac{2f_n^{(fit)}(\boldsymbol{X}) - f_n^{(obs)}}{\sigma_{fn}} \right)^2 + \left(\frac{f_{A1g}^{(fit)}(\boldsymbol{X}) - f_{A1g}^{(obs)}}{\sigma_{fA1g}} \right)^2. \tag{2}$$

The first term in eq. 2 is the weighted mean-square error of the second harmonic of the

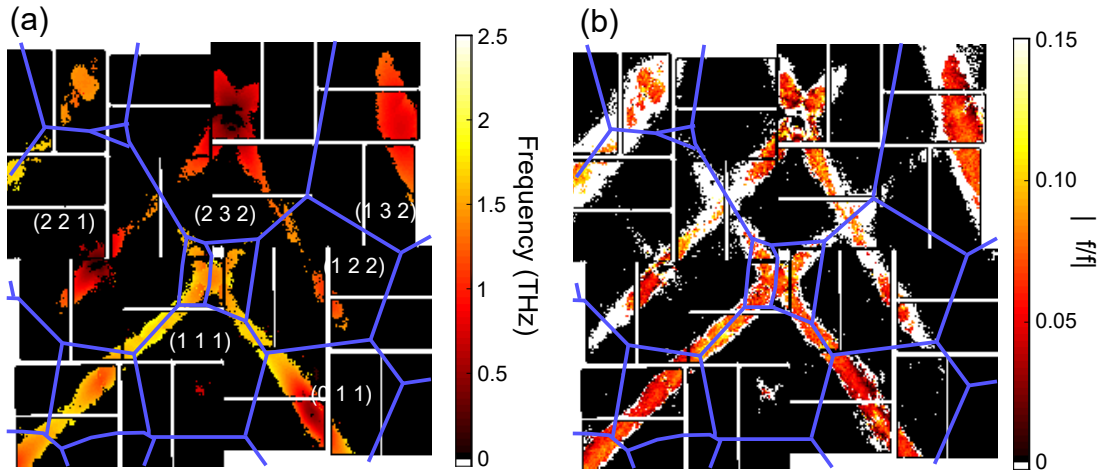

FIG. 2. (a) Dominant frequencies extracted from linear prediction fitting for every pixel where the maximum amplitude of the FFT frame passed the threshold of 0.1 (A.U.). Pixels in black are not fit. (b) Relative frequency change $\Delta f/f$ as a function of pixel.

computed phonon frequencies $2f_n^{(fit)}$, compared to the experimentally observed frequencies $f_n^{(obs)}$. The factor of two is present because the squeezing oscillations are observed at the second harmonic of the phonon frequency. The second term in the equation is the mean-square error of the A_{1g} mode frequency. We then minimize the mean-square error χ^2 as a function of the interatomic force parameters $\boldsymbol{X}$.

Each detector pixel is sensitive to six possible phonon branches, but the signal is strongest for the lower frequency modes polarized along the x-ray scattering wavevector, and thus only one of the acoustic phonon branches is typically observed. The LO and TO phonon branches away from zone center were not observed in our experiment. The observed oscillation frequency at each pixel was assigned to a phonon branch by selecting the branch with the highest computed thermal diffuse scattering (TDS) intensity [1, 2]. This assignment assumes similar excitation amplitude relative to equilibrium for all phonon modes, such that the oscillation amplitude is proportional to the initial mean-square displacement of the mode. The TDS intensity for each branch was computed in a similar manner to ref. [1]. For most pixels used in this fit, the fitted branch corresponds to one of the transverse acoustic modes.

When fitting the interatomic forces to a model, we must select the number of forces to vary. Our approach is to select the minimum number of forces to produce a reasonable convergence, in order to minimize any over-fitting or correlation between fit parameters.

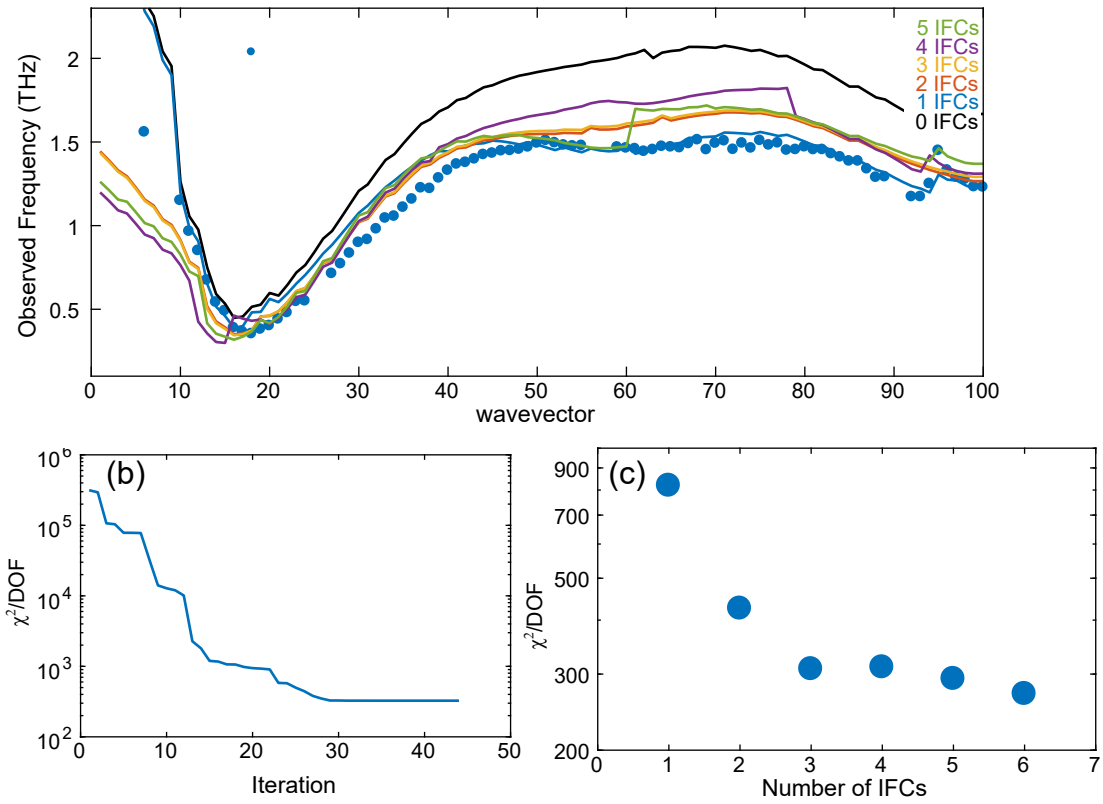

FIG. 3. (a) Fitting of the lineout shown in fig. 1 of the main text as a function of the number of IFC forces used. The black line is the results of the ground-state DFT calculation with no adjustable parameters. (b) Reduced χ^2 as a function of the iteration to minimize the mean-square error. The fitting converges after approximately 50 iterations. (c) Reduced χ^2 as a function of the number of adjustable IFCs (log y scale). Adjusting IFCs beyond the fourth does not significantly improve the fit. For reference, fitting the dispersion with no adjustable parameters is equivalent to the beginning of the fitting iteration in (b), with a reduced χ^2 of 3×10^5.

Therefore, we fit the cut of the dispersion shown in fig. 2(a) to three sets of forces (nine fit parameters). The fitting results along the line cut shown in fig. **??**(a) in the main text as a function of the number of adjustable forces used in the fit are shown in fig. 3(a). The dispersion produced from DFT calculations is shown in black (0 changed IFCs). The phonon dispersion produced by DFT calculations is higher frequency than the reconstructed dispersion across the Brillouin zone. By adjusting the nearest-neighbor forces, better agreement between the calculated and measured TA branch frequencies is reached. We can quantify this agreement by observing the mean-square error as a function of the number of inter-

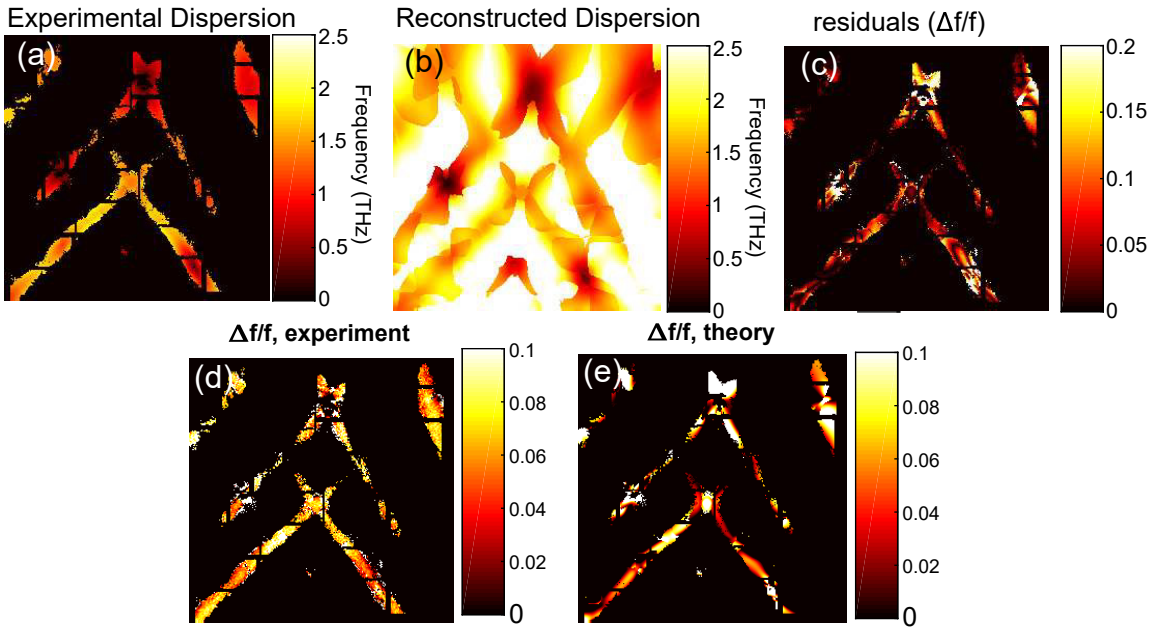

FIG. 4. (a) Fitted frequencies, as in fig. 2(a). (b) Results of the frequencies from the force fitting. (c) Residuals (fractional) from 0 to 20% of the frequencies relative to the fit. (d) Same in fig. 2(b). (e) Theoretical reconstruction of (d).

atomic force constant (IFC) matrices modified in the fitting, shown in fig. 3(c). Because the number of points fitted is much greater than the number of parameters used in the fit, information-theoretic approaches to determining the number of parameters are not appropriate for selecting the number of forces to fit.

For each incident laser fluence, the initial parameters were the full force constants derived from *ground-state* DFPT calculations. The minimization problem is solved by the constrained nonlinear optimizer algorithm in MATLAB. The algorithm converges to a minimum value in approximately 50 iterations. The descent of the algorithm to the minimized value is shown in fig. 3(b) for three IFCs.

The phonon dispersion is computed for each wavevector Q where the fitting converges, which is 7,080 pixels of the 65,536-pixel reduced pixel array. For each iteration, the dispersion is computed with the adjusted IFCs. The branches are then assigned by computing the diffuse scattering intensity of all six phonon branches, and taking the maximum for each pixel. The weighted mean-squared error is then assigned, and added to the mean-squared error from the A_{1g} mode. A general description for how to compute the diffuse scattering intensity for each phonon branch is described in ref. [1]; we follow a similar set of equations

for our analysis.

The absolute value of the residuals for the fitting routine are shown in fig. 4(c). The value varies from 0-20% of the observed frequency, depending on wavevector. A much higher precision fit can be obtained by only taking cuts along the high-symmetry directions, but at the cost of poor agreement away from high-symmetry directions.

Agreement between the reconstructed fit and experimentally observed frequency softening over reciprocal space is shown in fig. 4(d) and (e). In these panels, the softening is shown to be relatively independent of wavevector, though slightly higher near the zone boundaries. This is in rough agreement with our fitted model.

[1] R. Xu and T. C. Chiang, Zeitschrift für Kristallographie - Crystalline Materials **220**, 1009 (2005).

[2] C. B. Walker, Phys. Rev. **103**, 547 (1956).